

# Disturbance Observer Based Hovering Control of Quadrotor Tail-sitter VTOL UAVs Using $H_\infty$ Synthesis

Ximin Lyu, Jinni Zhou, Haowei Gu, Zexiang Li, Shaojie Shen, and Fu Zhang

**Abstract**—Hybrid VTOL UAVs such as tail-sitters allow several key maneuvers such as vertical takeoff, landing, and hovering while at the same time maintaining superior aerodynamic efficiency at level flight. However, the large wing area of a tail-sitter at hovering makes it rather sensitive to the cross wind. In this paper, we present a disturbance observer (DOB) based control method to improve its hovering accuracy in presence of external disturbances such as cross wind. The presented DOB, operating on top of the aircraft baseline position controller, is designed in frequency domain using  $H_\infty$  synthesis techniques and is guaranteed to stabilize the closed loop system with robustness to model uncertainties. In addition, it admits non-minimum phase system model, as the case of our tail-sitter platform, and does not require much hand tuning work on the  $Q$ -filter. Comparison study with existing UAV disturbance rejection method is conducted under different wind disturbances. Results show that the presented DOB control technique can effectively estimate various types of wind disturbances and lead to improved hovering accuracy of the tail-sitter UAV.

**Index Terms**—Aerial Systems; Mechanics and Control, Robust/Adaptive Control of Robotic Systems, Optimization and Optimal Control, DOB design methodology, Quadrotor tail-sitter UAV

## I. INTRODUCTION

IN recent years, Unmanned Aerial Vehicles (UAVs) have been widely used in the fields of aerial photography, surveying, monitoring, and patrol. In other scenarios such as precision agriculture, parcel delivery, etc., people are also attempting to employ UAVs to increase the efficiency and economy of their service. Motivated by this, the vertical takeoff and landing (VTOL) platform, which combines the maneuverability of a rotary-wing aircraft and the high level flight efficiency of a fixed-wing aircraft, attracts much attention recently. Among the various types of VTOL UAVs presented in [1], the tail-sitter VTOL aircrafts are perhaps the simplest implementation as they do not require extra actuators. Being simple is particularly useful for small scale UAVs in order to save weight and reduce manufacturing complexity. The tail-sitter vehicles take off and land on their tail, making hovering performances crucial in these phases by the wind disturbance,

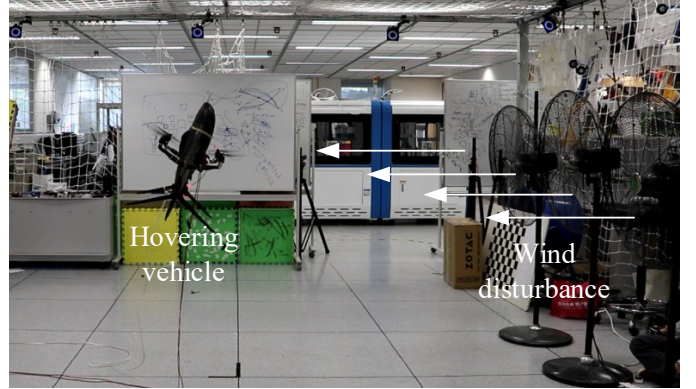


Fig. 1: The indoor experiments with wind disturbance. Video available at: <https://youtu.be/0BC5BkMuynM>

which is introduced by its large wing area. Poor hovering accuracy may further cause the aircraft fail to land at the desired location (e.g., load/unload the payload, charging, etc.), deteriorates its mission performance during hovering (e.g., precise monitoring), or even crash the aircraft (especially in the process of takeoff and landing).

Currently, several prototypes of tail-sitter UAVs have been developed. P. Sinha *et al.* [2] developed a tail-sitter named Quadshot, which consists of a flying wing with control surface and four rotors. A. Oosedo *et al.* [3] removed all the control surface and used only four rotors for both hovering and level flight control. This work mainly focuses on optimizing the transition from hovering flight to level flight. R. H. Stone *et al.* [4] developed a twin-engine T-wing tail-sitter UAV. The outdoor hovering flight tests were conducted, which showed that the hovering accuracy is not satisfactory. R. Bapst *et al.* [5] developed a similar but smaller twin engine tail-sitter prototype without mentioning the wind disturbance issues. Later on, S. Verling *et al.* [6] developed a similar dual-rotor tail-sitter UAV and did the verification experiments. The anti-wind issues were mentioned as a future work. After that, Y. Demitri *et al.* [7] from the same group proposed a model-based wind estimator for tail-sitter UAV at hovering, which could be helpful for autonomous landing and energy optimized hovering in steady cross wind situation. However, it did not consider the hovering accuracy. R Ritz *et al.* [8] proposed a global controller for flying wing tail-sitter, the hovering accuracy issues are also not considered.

Comparing with the dual rotor tail-sitter, the quadrotor tail-sitter has better anti-wind performance [1]. In our previous

Manuscript received: Feb, 10th, 2018; Revised May, 2nd, 2018; Accepted June, 1st, 2018.

This paper was recommended for publication by Editor Jonathan Roberts upon evaluation of the Associate Editor and Reviewers' comments. This work was supported by Hong Kong ITF Foundation (ITS/334/15FP)

All authors are with the Department of Electronic and Computer Engineering, Hong Kong University of Science and Technology, Hong Kong, China. xlvaa@connect.ust.hk, eefzhang@ust.hk

Digital Object Identifier (DOI): see top of this page.

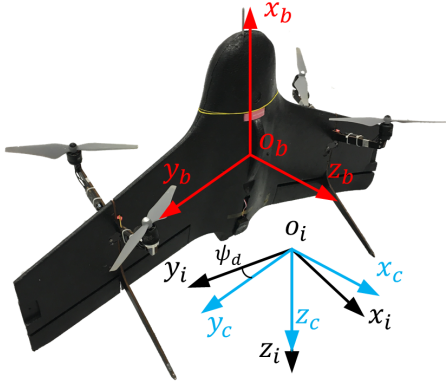


Fig. 2: The quad-rotor tail-sitter UAV coordinate system

work, we have designed and implemented two quadrotor tail-sitter prototypes. The indoor experiments were conducted to show that the aircraft remains stable in presence of cross wind [9]. The outdoor flight experiments were conducted to show that our vehicle can accomplish fully autonomous flight including vertical takeoff, transition, level flight and landing [10, 11]. However, the existing baseline controller can still not achieve the sufficient level of hovering accuracy of the vehicle.

Disturbance observer (DOB), as a powerful tool for disturbance estimation and compensation [12], has received wide industrial applications, such as transport aircrafts [13], surgical devices [14], hard disks [15], etc. There are also various types of DOBs applied to UAVs. S. H. Jeong *et al.* [16] proposed an acceleration based DOB for the attitude control of a quadrotor UAV. H. Wang *et al.* [17] proposed a linear dual DOB on attitude control with attention restricted in tracking control of quadrotor UAVs. As can be seen, these work are all motivated by the attitude control of quadrotor UAVs. In contrast, S. J. Lee *et al.* [18] proposed a DOB structure for the position control of a hexarotor UAV. The method followed typical design procedures, such as plant inverse and low pass filtering, of conventional DOB design methodologies, but extended to the nonlinear dynamics of hexarotor UAVs. M. R. Mokhtari *et al.* [19] proposed a disturbance observer with finite time convergence (FTDO). The simulation results show that the tracking accuracy degrades with the adding of sensor noise.

In this paper, we propose to use a velocity DOB with the design method inspired by [15], but additionally consider measurement noise in actual UAVs, to estimate and compensate the wind disturbance of a quadrotor tail-sitter VTOL UAV at hovering flight. Our contribution in this work lies in twofold: (1) an ease to tune disturbance observer (DOB) design methodology, and applying such DOB design methods to UAVs to produce (2) improved hovering accuracy of quadrotor tail-sitter VTOL UAVs operating in cross wind, which is a long standing problem for tail-sitter VTOL UAVs. The novelty of the proposed method lies in that it considerably mitigates human tuning effort in conventional DOB design by utilizing  $H_\infty$  optimal control theory. Furthermore, it is applicable to non-minimum phase systems with measurement noise and returns the optimal, stable plant inverse and  $Q$  filter with guaranteed closed loop stability; Finally, the proposed method

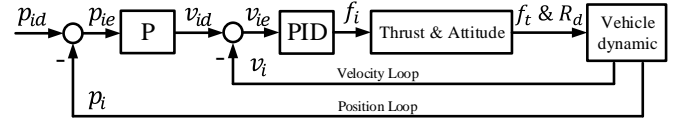


Fig. 3: The position controller diagram

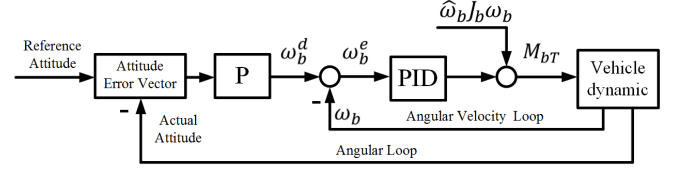


Fig. 4: The attitude controller diagram

provides the ability to mitigate the effect of measurement noise, which commonly exists in actual UAVs.

The remainder of this paper is organized as follows: Sec. II introduces the vehicle dynamic model and the baseline feedback controller. In Sec. III, we will present the proposed DOB design method and their application in a quadrotor tail-sitter VTOL UAV model. Experiments are supplied in Sec. IV. Sec. V draws conclusions and discusses future work.

## II. MODELING AND BASELINE FEEDBACK CONTROL

The coordinate frames of our tail-sitter UAV are shown in Fig. 2: the body frame  $x_b, y_b, z_b$ , the inertial frame  $x_i, y_i, z_i$ , and the intermediate frame  $x_c, y_c, z_c$ . The origin  $o_b$  of the body frame is set to coincide with the vehicle's center of gravity. The intermediate frame is defined through rotating along  $z_i$  by  $\psi_d$ , the desired yaw angle when the vehicle is hovering. Rotation along body axis  $x_b, y_b$ , and  $z_b$  are respectively called roll, pitch, and yaw. The roll, pitch, and yaw angles are respectively denoted by  $\phi, \theta$ , and  $\psi$ .  $Z-X-Y$  Tait-Bryan angles are used to represent the vehicle attitude to prevent the singularity point at pitch angles equal to  $\pm 90^\circ$ , which are commonly experienced angles on tail-sitter vehicles [20].

### A. Modeling

The equation of motion of the tail-sitter UAV can be written as [9]

$$\begin{bmatrix} mI & 0 \\ 0 & J_b \end{bmatrix} \begin{bmatrix} \dot{v}_i \\ \dot{\omega}_b \end{bmatrix} + \begin{bmatrix} 0 \\ \hat{\omega}_b J_b \omega_b \end{bmatrix} = \begin{bmatrix} R f_{ba} \\ M_{ba} \end{bmatrix} + \begin{bmatrix} f_{ig} \\ 0 \end{bmatrix} + \begin{bmatrix} R f_{bT} \\ M_{bT} \end{bmatrix} \quad (1)$$

$$\dot{R} = R \cdot \hat{\omega}_b$$

where  $m$  is mass,  $I \in \mathbb{R}^{3 \times 3}$  is the identity matrix. In all notations, the subscript notation “ $b$ ”, “ $c$ ”, and “ $i$ ” are respectively used to denote the body frame, intermediate frame, and inertial frame. In addition, the first subscript is always used to denote the coordinate frame, followed by other subscripts that carries further information. For example,  $J_b \in \mathbb{R}^{3 \times 3}$  is inertial matrix in the body frame,  $\omega_b \in \mathbb{R}^3$  is angular velocity in the body frame,  $f_{ba} \in \mathbb{R}^3$  and  $M_{ba} \in \mathbb{R}^3$  are respectively the aerodynamic force and moment vector in the body frame.  $f_{bT} \in \mathbb{R}^3$  and  $M_{bT} \in \mathbb{R}^3$  are respectively force and moment vectors produced by rotors in the body frame.  $v_i \in \mathbb{R}^3$  is vehicle velocity in the inertial frame.

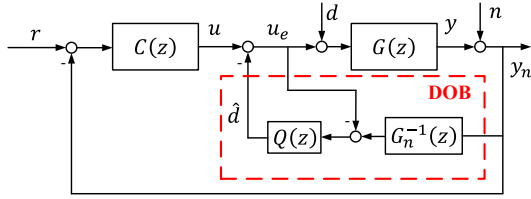


Fig. 5: A general system with conventional DOB

$f_{ig} = [0 \ 0 \ mg]^T \in \mathbb{R}^3$  is the gravity in the inertial frame,  $R \in \mathbb{R}^{3 \times 3}$  is the rotation matrix from body frame to inertial frame, the hat map  $\hat{\cdot}$  is defined such that  $\hat{x}y = x \times y$  for any  $x, y \in \mathbb{R}^3$ . The motor gyroscopic effect and motor acceleration and deceleration terms are neglected as they are usually very small.

### B. Controller structure

The controller structure of our vehicle is explained in [10] in detail. In this paper, we will focus on the hovering flight of the vehicle in rotary-wing mode. Thus, only the rotary-wing position controller (runs at  $\frac{250}{3}$  Hz) and tail-sitter attitude controller (runs at 250 Hz) are used. The rotary-wing position controller is a cascaded controller implemented in inertial frame as shown in Fig. 3.

The position loop is a proportional controller and the velocity loop is a PID controller. Through the *Thrust & Attitude* module, the inertial force vector  $f_i$  was transformed to vehicle thrust  $f_t$  and desired attitude  $R_d$  [21]. The vehicle thrust can be calculated by

$$f_t = f_i \cdot x_b \quad (2)$$

and the desired attitude is computed as

$$\begin{aligned} x_b^d &= \frac{f_i}{\|f_i\|} \\ y_c^d &= [-\sin(\psi_d) \ \cos(\psi_d) \ 0]^T \\ z_b^d &= \frac{x_b^d \times y_c^d}{\|x_b^d \times y_c^d\|} \\ y_b^d &= z_b^d \times x_b^d \\ R_d &= [x_b^d \ y_b^d \ z_b^d] \end{aligned} \quad (3)$$

where  $x_b^d, y_b^d$ , and  $z_b^d$  are desired body axis vectors represented in inertial frame,  $y_c^d$  is the desired intermediate axis vector represented in inertial frame. After that, the desired attitude is fed to the cascaded tail-sitter attitude controller as shown in Fig. 4. The *Linear Quaternion* method presented in [10] is used to calculate the attitude error. Thus the attitude can be well decoupled and controlled independently in roll, pitch, and yaw directions.

### III. DOB DESIGN

The conventional DOB structure of a general system is shown in Fig. 5, where  $C(z)$  is the baseline controller;  $G(z)$  is the system plant;  $G_n(z)$  is the nominal plant;  $Q(z)$  is usually a low pass filter to guarantee the robustness of the DOB module and the causality of  $Q(z)G_n^{-1}(z)$  such that it can be implemented.  $r$  is the reference signal;  $u$  is the controller output;  $d$  is the disturbance to the system;  $\hat{d}$  is

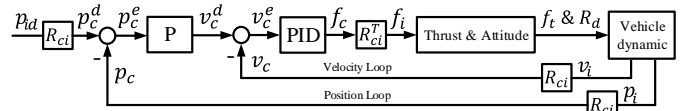


Fig. 6: Position controller in intermediate frame

the disturbance estimate;  $u_e = u - \hat{d}$  is the control signal of the plant;  $y$  is the plant output;  $n$  is the measurement noise. The basic idea of the DOB is to utilize the plant output to reconstruct the plant input, which consists of control signal  $u_e$  and disturbance  $d$ , and subsequently subtract it by the control signal  $u_e$  to produce the disturbance estimate. The estimated disturbance, after filtered by the low pass filter  $Q(z)$ , is then used to compensate the controller output  $u$ . Such a relationship is easily described by its transfer function shown below [15]

$$\hat{d} = \frac{Q(G_n^{-1}G + GC)(1 + GC)^{-1}}{(1 - Q) + Q(G_n^{-1}G + GC)(1 + GC)^{-1}}d \quad (4)$$

where  $z$  is omitted for simplicity. Note that if

$$\begin{aligned} Q(z) &= 1 \\ G_n^{-1}(z)G(z) &= 1 \end{aligned} \quad (5)$$

we have  $\hat{d} = d$ , which means the DOB can perfectly estimate the disturbance.

#### A. Linearized system model

To design the presented disturbance observer, we need a frequency domain model of the VTOL UAV. Regarding the aerodynamic force  $f_{ba}$  and moment  $M_{ba}$  in (1) as lumped disturbances caused by cross wind, the system model can be rewritten as

$$\begin{aligned} m\dot{v}_{ix} &= (\cos\theta\cos\psi - \sin\phi\sin\theta\sin\psi)f_t + d_{ix} \\ m\dot{v}_{iy} &= (\cos\theta\sin\psi + \sin\phi\sin\theta\cos\psi)f_t + d_{iy} \\ m\dot{v}_{iz} &= -\cos\phi\sin\theta f_t + mg + d_{iz} \end{aligned} \quad (6)$$

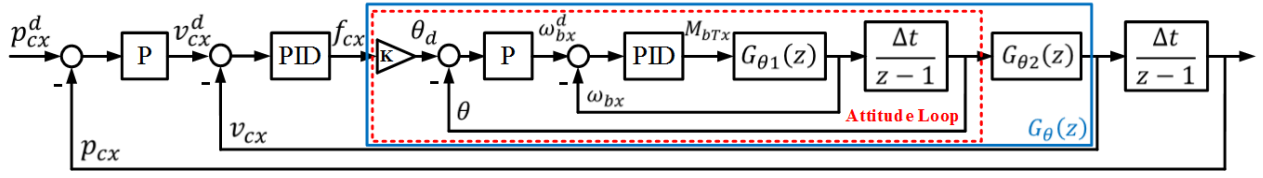
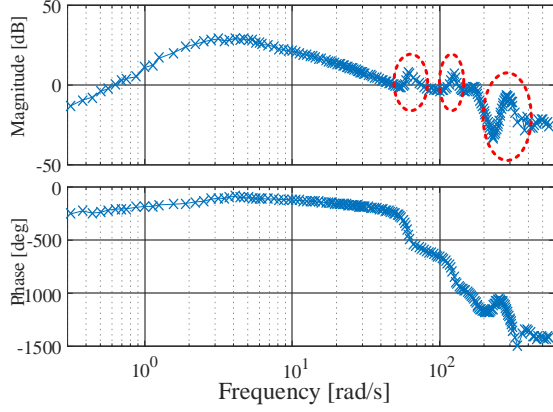
To obtain a frequency domain model of the vehicle, we linearize the system at its hovering condition where  $\phi = 0$ ,  $\theta = \frac{\pi}{2}$ ,  $\psi = \psi_d$ , and  $f_t = mg$ . The linearized model is

$$\begin{bmatrix} \dot{v}_{ix} \\ \dot{v}_{iy} \\ \dot{v}_{iz} \end{bmatrix} = g \begin{bmatrix} -s\psi_d & c\psi_d & 0 \\ c\psi_d & s\psi_d & 0 \\ 0 & 0 & -1 \end{bmatrix} \begin{bmatrix} \phi \\ \frac{\pi}{2} - \theta \\ \frac{f_t}{mg} \end{bmatrix} + \begin{bmatrix} 0 \\ 0 \\ g \end{bmatrix} + \begin{bmatrix} \frac{d_{ix}}{m} \\ \frac{d_{iy}}{m} \\ \frac{d_{iz}}{m} \end{bmatrix} \quad (7)$$

where  $s(\cdot)$  and  $c(\cdot)$  abbreviates  $\sin(\cdot)$  and  $\cos(\cdot)$ , respectively. From (7), we can see that the acceleration in inertial frame is the combination of roll and pitch angle, which is coupled by the yaw angle. To decouple their control, we represent our position controller as well as the system model in intermediate frame as shown in Fig. 6. Representing all translational velocities in intermediate frame yields

$$\begin{aligned} \begin{bmatrix} \dot{v}_{cx} \\ \dot{v}_{cy} \\ \dot{v}_{cz} \end{bmatrix} &= R_{ci} \begin{bmatrix} \dot{v}_{ix} \\ \dot{v}_{iy} \\ \dot{v}_{iz} \end{bmatrix} = g \begin{bmatrix} \frac{\pi}{2} - \theta \\ \phi \\ 1 - \frac{f_t}{mg} \end{bmatrix} + \frac{R_{ci}d_i}{m} \\ R_{ci} &= \begin{bmatrix} c\psi_d & s\psi_d & 0 \\ -s\psi_d & c\psi_d & 0 \\ 0 & 0 & 1 \end{bmatrix} \end{aligned} \quad (8)$$

where the acceleration along  $x_c$  and  $y_c$  axis (i.e.,  $\dot{v}_{cx}$  and

Fig. 7: Linearized system in  $x_c$  directionFig. 8: System identification of  $G_{\theta_1}(z)$  in frequency domain

$\dot{v}_{cy}$ ) only relates to pitch angle and roll angle, respectively. Accordingly, the controller presented in Sec. II-A can be linearized in a similar way. The linearized system model and controller along  $x_c$  direction are summarized in Fig. 7. As the system along  $x_c$  and  $y_c$  direction are very similar, we will take the  $x_c$  direction as an example to demonstrate the DOB design process for simplicity.

In Fig. 7, the output gain  $K$  converts the desired force  $f_{cx}$  to the desired pitch angle  $\theta_d$ ,  $G_{\theta_1}(z)$  denotes the dynamic model from moment to angular velocity, and  $G_{\theta_2}(z)$  is the model from pitch angle to velocity in  $x_c$  direction. Ideally,  $K = \frac{1}{mg}$ ,  $G_{\theta_1}(z)$  and  $G_{\theta_2}(z)$  are both integral actions. However, as the UAV body and motor arms are not strictly rigid, there exist flexible modes in  $G_{\theta_1}(z)$ . Other factors such as controller delay, aerodynamic damping will also cause the actual dynamic model  $G_{\theta_1}(z)$  far more complicated than an integral action. To best see the detailed dynamics of  $G_{\theta_1}(z)$ , we identify the vehicle's angular velocity by a frequency sweep method outlined in [22]. The identified system frequency response is shown in Fig. 8. It is seen that at the frequency range from 4 to 50 rad/s, there is an integral mode corresponding to our first principle integral model, while at the high frequency range from 50 to 600 rad/s, there are three flexible modes. Similarly, the dynamic model  $G_{\theta_2}(z)$ , which denotes the model from pitch angle to translational velocity, is ideally  $\frac{g\Delta t}{z-1}$ .

Due to the complicated wing aerodynamic forces as well as flexible modes in the translational dynamics, the actual model is also much more complicated than we expected. Therefore, in practice, the entire model from  $f_{cx}$  to  $v_{cx}$  i.e.,  $G_{\theta}(z)$  is identified, instead of identifying  $G_{\theta_1}(z)$  and  $G_{\theta_2}(z)$ , separately. Different from the angular velocity case, we perform the system identification on our simulated platform presented in [20], which captures many details of the actual VTOL UAV dynamics including motor saturation, delay, aerodynamic force

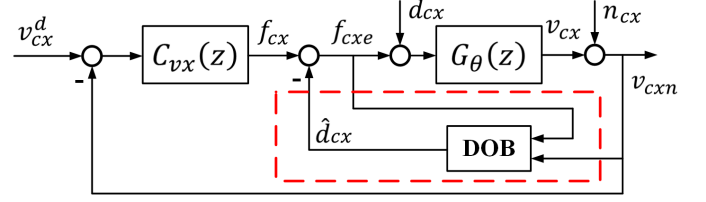


Fig. 9: Linearized system with DOB

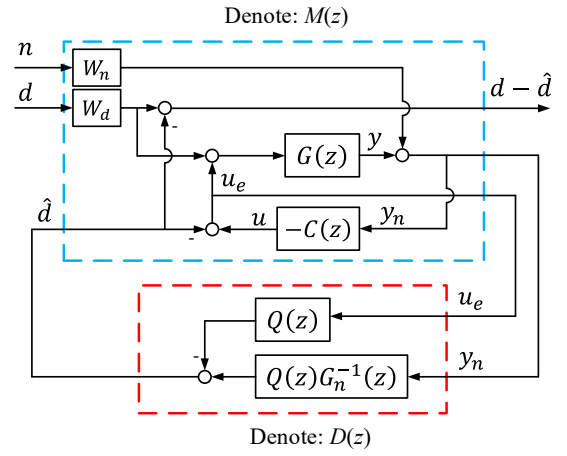


Fig. 10: Equivalent representation for the system in Fig. 5

and moments, etc., but not flexible modes. The designed DOB based on the simulation model turned out work for the real system quite well, possibly because the flexible modes is much higher than the bandwidth of the disturbance observer nearing hovering state. Based on the frequency response data obtained in the simulator, the fitted transfer function is

$$G_{\theta}(z) = \frac{0.0055547(z + 3.184)(z - 0.5806)(z + 0.2115)}{(z - 0.412)(z - 0.929)(z - 1)(z^2 + 0.0307z + 0.0495)} \quad (9)$$

which is a non-minimum phase system due to the unstable zero  $z = -3.184$ . After getting  $G_{\theta}(z)$ , the velocity loop with DOB can be simplified as shown in Fig. 9, where  $C_{vx}(z)$  represents the translational velocity PID controller in Fig. 7.

### B. $H_{\infty}$ DOB design method

As we mentioned in Sec. III-A,  $G_{\theta}(z)$  is a non-minimum phase system, causing the plant inverse in conventional DOB design method to be unstable. Various methods have been proposed to fix this issue. N. H. Jo *et al.* [23] presented a new DOB configuration by adding a new filter without considering the effects of sensor noise. According to our simulation results, the DOB designed using this method is too sensitive to the measurement noise to implement on our system. H. T. Seo *et al.* [24], proposed an  $H_{\infty}$  based DOB design method for



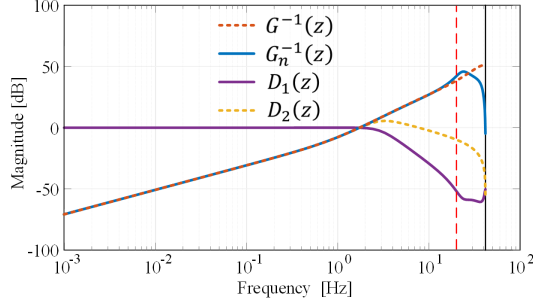


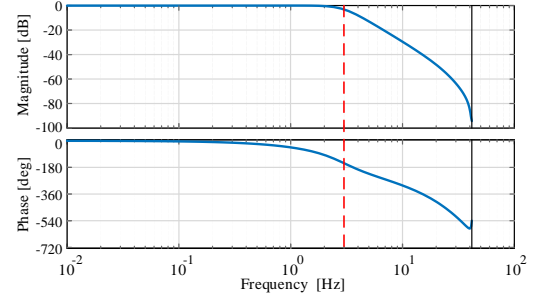
Fig. 11: Bode diagram of the DOB design results

single input single output (SISO) systems, including the non-minimum phase systems. However, this design method is based on the system plant solely and the closed loop system stability can not be guaranteed. Another feasible solution is to find an alternative stable inverse satisfying  $G_n^{-1}(z)G(z) \approx 1$  [15]. However, this method requires much human work on tuning the appropriate filters or manually finding a stable plant inverse that approximates the true inverse. In this paper, we adopt the  $H_\infty$  based DOB design method recently introduced in [15], which utilizes systematic optimal control theory to find the optimal DOB controller that minimizes the  $H_\infty$  norm of the weighted transfer function from disturbance to its estimation error. The formed DOB design problem becomes a standard  $H_\infty$  optimal control problem and can be solved by means of Linear Matrix Inequality (LMI) [15]. It has been shown in the optimal control theory that the synthesized DOB controller will be guaranteed to be both optimal and stable. However, in the original work by Zheng, *et al.* [15], no noise was considered. The synthesized DOB, according to our simulation verification, can successfully approximate an optimal plant inverse of the system, but considerably amplify the measurement noise, which is prevalent in actual UAV systems. In this paper, we adopt this  $H_\infty$  based DOB controller design methodology and add a second channel to further attenuate the noise. With the second channel, the original system for DOB design in Fig. 5 can be equivalently transformed into Fig. 10 (assuming  $W_n = W_d = 1$ ), where the upper part, denoted by  $M(z)$ , is the baseline feedback control loop and the lower part, denoted by  $D(z) = [D_1(z), D_2(z)]$ , is the disturbance observer to be designed with two inputs (i.e. measurement and total control input) and one output (i.e. the estimated disturbance). Comparing with the original DOB structure in Fig. 5, we see that  $D_1(z) = -Q(z)$  and  $D_2(z) = Q(z)G_n^{-1}(z)$  as shown in Fig. 10. The  $H_\infty$  based DOB design method then attempts to find an optimal feedback controller ( $D(z)$  in this case) that minimizes the  $H_\infty$  norm from  $[n, d]^T$  to  $d - \hat{d}$ , i.e.

$$\min_{D(z)} \|G_L(M, D)\|_\infty \quad (10)$$

where  $G_L(M, D)$  denotes the lower linear fractional transform [25]. After obtaining the DOB controller  $D(z)$ , we can reconstruct the  $Q$ -filter and nominal plant inverse by  $Q(z) = -D_1(z)$  and  $G_n^{-1}(z) = -D_1(z)^{-1}D_2(z)$  respectively to compare them with conventional DOB controller structure.

$W_d$  and  $W_n$  are respectively the weighting functions that penalizes the disturbances and noises in certain frequency

Fig. 12: Bode diagram from  $d$  to  $\hat{d}$ 

ranges, which are used in the DOB design process. As our primary goal is to attenuate the wind disturbances acting on the VTOL UAV, which is typically concentrated on low frequency range, while the measurement noise is usually at high frequency range. Thus, the weighting functions are respectively designed as

$$\begin{aligned} W_n &= \frac{34.67z - 34.65}{z + 0.3068} \\ W_d &= \frac{0.02885z + 0.00885}{z - 0.9996} \end{aligned} \quad (11)$$

where  $W_n$  and  $W_d$  are respectively high pass and low pass filter with the cut-off frequency chosen empirically according to the frequency region of disturbance and noise in our platform. It is worth of mentioning that the two weighting filters are only used in synthesizing the DOB. When implementing the synthesized DOB, no weighting filter will be used as shown in Fig. 5 and Fig. 9.

### C. DOB design results

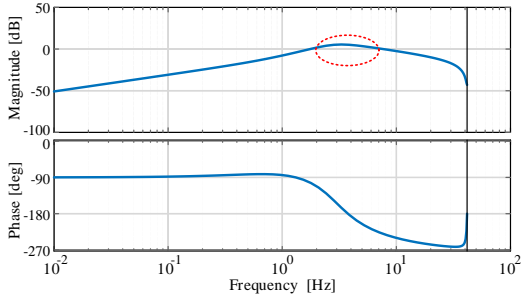
Before proceeding to the actual test of the designed DOB controller, we analyze their performance in frequency domain. Fig. 11 shows the synthesized DOB controller (i.e.  $D_1(z)$  and  $D_2(z)$ ) and the reconstructed plant inverse. It is seen that the reconstructed plant inverse matches the actual plant inverse (non-causal and unstable) very well over low frequencies up to 20 Hz (see Fig. 11).

Fig. 12 shows the bode diagram of the frequency response from external disturbance  $d$  to DOB output  $\hat{d}$ . It can be seen that the frequency response is almost equal to 1 over low frequencies up to 2 Hz, meaning that the DOB controller can accurately estimate the external disturbances over these frequencies. Furthermore, the 2 Hz disturbance bandwidth is quite sufficient to cover the cross wind considered in this paper.

Finally, the frequency response from noise  $n$  to the disturbance estimate  $\hat{d}$  is shown in Fig. 13. It can be seen that the noise is well attenuated over a wide range of frequencies. The very narrow frequency range from 2 Hz to 6 Hz (see Fig. 13) over which the noise is slightly amplified show little effect on the overall performance.

## IV. EXPERIMENT VERIFICATION

To verify the performance of the designed DOB, we conduct several indoor experiments, as shown in Fig. 1. A motion

Fig. 13: Bode diagram from  $n$  to  $\hat{d}$ 

capture system is used to provide the aircraft position and heading information. All the states (namely, position, velocity, acceleration, attitude, etc.) mentioned below come from the *position\_estimator\_inav* and *attitude\_estimator\_q* modules in PX4 firmware [26]. Four fans are used to produce the wind disturbance, whose velocity is up to 5.6 m/s (the wind speed is measured by using a handheld vane anemometer known as Testo 410-1) at the hovering point of the vehicle (i.e., roughly 2 m away from the fans and 1.35 m up the ground). The experiment consists of four stages. In the first two stages, only the aircraft baseline position controller presented in Sec. II is used, while in the last two stages the DOB (designed by either our proposed approach or the method in [18] for comparison study) is also enabled for disturbance estimation and compensation. For each tested case, two types of wind disturbances are created: a sudden constant wind and a periodic wind. The constant wind disturbance is produced by turning on the four fans simultaneously for 30 s. And the periodic wind disturbance is produced by alternatively turning on and off the fans for 10 s.

To validate the effectiveness of the proposed DOB design method, a comparison study with the method in [18] is conducted. The disturbance observer in [18] follows the standard disturbance observer design structure (i.e. Fig. 5) but uses a simplified plant model that is always invertible, eliminating the need for inverting non-minimal phase plant dynamics. Following the procedure in [18], the simplified plant model (i.e. attitude dynamics model) can be written as

$$\Lambda_{n,a,i}(s) = \frac{q_i(s)}{q_{d,i}(s)} = \frac{PID \frac{P}{J_{b_{ii}} s^2}}{1 + PID \frac{1}{J_{b_{ii}} s} + PID \frac{P}{J_{b_{ii}} s^2}} \quad (12)$$

where  $P$  and  $PID$  are respectively the proportional controller and PID controller as shown in Fig. 4.

For the design of  $Q$ -filter, [18] suggests using the below form when  $\Lambda_{n,a,i}(s)$  has relative degree  $r$ :

$$Q(s) = \frac{b_k(\tau s)^k + b_{k-1}(\tau s)^{k-1} + \dots + b_0}{(\tau s)^l + a_{l-1}(\tau s)^{l-1} + \dots + a_1(\tau s) + a_0} \quad (13)$$

where  $l \geq k + r$  and  $b_0 = a_0$ .  $\tau$  is used to tune the robustness of the disturbance observer. A higher  $\tau$  value makes the system more robust but causes poor disturbance rejection. In our implementation, we set  $k = 0$ ,  $l = 2$ ,  $a_0 = b_0 = 1$ ,  $a_1 = 2$ , which are same with the parameter from [18]. When tuning the parameter  $\tau$ , we noticed that the aircraft vibrates for very small  $\tau$ , possibly due to the poor robustness of the disturbance

TABLE I: DOB designed by [18]

|                      | Stage_1  | Stage_2  | Stage_3  | Stage_4  |
|----------------------|----------|----------|----------|----------|
| Start Time (s)       | 54,122   | 128,202  | 217,270  | 285,353  |
| DOB                  | OFF      | OFF      | ON       | ON       |
| Wind Type            | Constant | Periodic | Constant | Periodic |
| Mean Error (m)       | 0.171    | 0.265    | 0.111    | 0.144    |
| Max Position Neg (m) | -0.616   | -0.627   | -0.383   | -0.397   |
| Max Position Pos (m) | 0.695    | 0.478    | 0.373    | 0.247    |

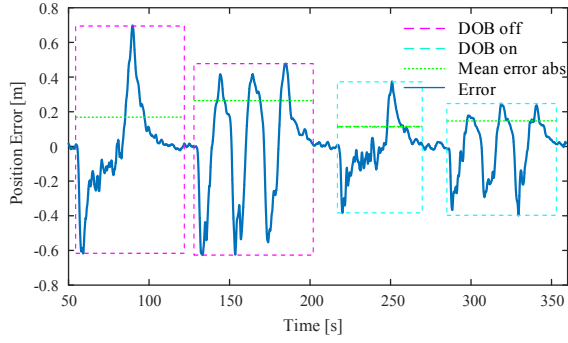
TABLE II: DOB designed by  $H_\infty$ 

|                      | Stage_1  | Stage_2  | Stage_3  | Stage_4  |
|----------------------|----------|----------|----------|----------|
| Start/End Time (s)   | 65,121   | 139,212  | 231,268  | 291,346  |
| DOB                  | OFF      | OFF      | ON       | ON       |
| Wind Type            | Constant | Periodic | Constant | Periodic |
| Mean Error (m)       | 0.193    | 0.243    | 0.028    | 0.039    |
| Max Position Neg (m) | -0.443   | -0.470   | -0.106   | -0.141   |
| Max Position Pos (m) | 0.628    | 0.422    | 0.130    | 0.134    |

observer as suggested in [18]. To make the comparison fair, we start the parameter  $\tau$  from a very small value and gradually increase it until the system does not vibrate. This leads to the best disturbance rejection performance while still maintaining the system stability.

Fig. 14 shows the experiment results of method in [18] (Fig. 14 (a)) and our proposed method (Fig. 14 (b)). Magenta rectangle and cyan tangle are respectively used to label the first two stages with DOB turned off and the rest two stages with DOB turned on. We consider the turning on the fans as the beginning of a stage and the position error less than 1 cm after turning off the fans as the end of a stage. Thus, the width of a rectangle represents the duration of a stage. The top line and bottom line of the rectangle respectively represents the maximum position error along positive and negative  $x_c$  axis during a stage. The green dotted linear represents the mean value of the absolute position error that is defined as the absolute value of the position error during a stage.

Referring to Fig. 14 (a), which shows the experimental results with method of [18], the vehicle was hovering at a stationary point with the DOB turned off. Starting from 54 s (stage 1), the four fans were turned on simultaneously and the vehicle was blown away for -0.616 m. After that, the vehicle gradually converges to the initial point. 30 s later, four fans were turned off and 0.695 m position error was observed, which is caused by the delay of the integrator in the baseline position controller. The corresponding mean value of the absolute position error was 0.171 m. After the vehicle re-stabilizes itself back to the initial hovering point, the periodic wind was added (stage 2). During this stage, the position error was from -0.627 m to 0.478 m and the mean value of the absolute position error was 0.265 m. Starting from 217 s (i.e., the third stage), the 30 s constant wind was added again but with the DOB designed by [18] turned on. The position error was from -0.383 m to 0.373 m and the mean value of the absolute position error was 0.111 m. Comparing to stage one, where only the baseline position controller is used, the position accuracy with the DOB of [18] in maximum positive position error, negative position error and mean value of the absolute position error are respectively improved by 1.86, 1.61, and



(a) DOB designed by [18]

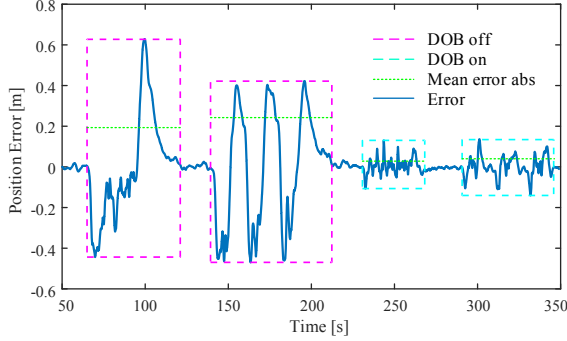
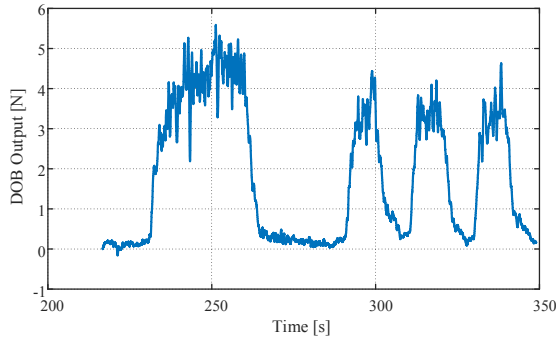
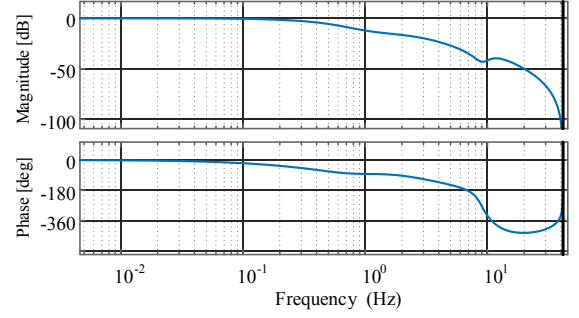
(b) DOB designed by  $H_\infty$ 

Fig. 14: Comparative experiment results

Fig. 15: DOB output designed by  $H_\infty$ 

1.54 times. The fourth stage started at 285 s, the position error is from -0.397 m to 0.247 m and the corresponding mean error is 0.144 m. Similarly, the position accuracy in maximum positive position error, negative position error and mean value of the absolute position error are respectively improved by 1.94, 1.58, and 1.84 times when compared to its baseline position controller in stage two. Table I summarizes the experimental results.

Fig. 14 (b) shows the flight log data of the position error along  $x_c$  direction by using the DOB designed by our method. The position error of first stage and second stage (labeled by magenta rectangle) are very similar to that of Fig. 14 (a). This shows that by hovering at a preset position, the added wind disturbance (both constant wind and periodic wind) are very similar. As for the stage three, the position error is from -0.106 m to 0.130 m and the mean error is 0.028 m. It is seen that by adding the DOB designed by our proposed method, the position accuracy in maximum positive position error,

Fig. 16: Bode diagram from  $d$  to  $\hat{d}$  by [18]

negative position error and mean value of the absolute position error are respectively improved by 4.75, 4.18, and 6.89 times when compared to the baseline controller in stage one. For the stage four, the position error is from -0.141 m to 0.134 m. The corresponding mean error is 0.039 m. Compared to the baseline controller in stage two, the position accuracy is improved by 4.83, 4.18, and 6.89 times, respectively. All the performance data are summarized in Table II. Fig. 15 shows the estimated disturbance with our designed DOB during the third and fourth stage, which shows the estimated force produced by the constant wind and periodic wind. It is seen that the disturbance observer is very responsive. Due to the lack of ground truth wind force, the estimation accuracy can't be assessed directly.

As we can see from the test results, when compared to the method in [18], the proposed disturbance observer designed by  $H_\infty$  technique can improve the hovering accuracy of our tail-sitter VTOL UAV by 2.49, 2.65, and 3.74 times for constant wind and 2.55, 2.60, and 4.47 times for periodic winds respectively in maximum positive position error, negative position error and mean value of the absolute position error. The possible reasons are as follows: (1) the actual attitude dynamics is non-minimum phase, which is much more complicated than the simplified plant model used in [18]. This model mismatch could lead to disturbance estimation error; (2) the specific  $Q$ -filter structure in [18] is not necessarily optimal. Fig. 16 shows the bode diagram from disturbance to its estimate for the method of [18]. When compared with Fig. 12, we can see that the DOB designed by our method has higher bandwidth in estimating the external disturbance, which explains the superior disturbance estimation and compensation performance of our proposed method.

Finally, it is worth of mentioning that, comparing with the results in [18], we find that our re-implementation of the DOB from [18] are slightly worse than the original results presented in [18], due to the following two reasons: (1) the disturbance rejection performance really depends on both the baseline controller and add-on disturbance observer. Though we re-implemented the same disturbance observer as that of [18], the baseline controller is quite different due to the difference between the hexarotor used in [18] and the homemade tail-sitter VTOL UAV used in this paper (e.g., lower flexible modes, higher noise and system delay, etc.). Indeed, the bandwidth of our baseline controller, limited by the noise and flexible modes of such a homemade tail-sitter, is lower

than that of [18]. Thus, the resulting hovering accuracy of our system (see Fig. 14 (a) from 54 s to 122 s) is slightly worse than that of [18] (see left part of Fig. 10 in [18]) when no DOB is used in both cases. (2) the wind disturbance used in our work has different effect from the exogenous disturbance produced manually in [18]. For example, wind disturbance not only produces a disturbance force, but also introduce a damping effect which, in turn, change the location of poles of the aircraft transfer function.

## V. CONCLUSION AND FUTURE WORK

In this paper, we focus on dealing with the wind disturbance on our tail-sitter platform by adding a DOB to the baseline feedback position controller. The system was linearized along  $x_c$  and  $y_c$  directions of the intermediate frame and its model is identified using frequency sweep method. We found that the translational dynamics of the tail-sitter UAV along  $x_c$  is non-minimum phase. To cope with this situation, a  $H_\infty$  DOB design method, which can be used for a general SISO system with measurement noise, was proposed and implemented on our platform. Indoor experiments on  $x_c$  directions were conducted to show that our designed DOB can effectively improve the position control performance and has a better performance than that designed by [18]. Future work lies in designing dual-loop DOB which could compensate both external force and moment disturbance (e.g., external force hitting only on one wing). Currently, a motion capture system is used to provide accurate position and velocity feedback. Future work will focus on implementing the DOB in an outdoor environment without motion capture. The performance of a DOB relies on the quality of feedback information. One possible way is to add vision sensors to obtain accurate feedback in the outdoor environment and the parameter of weighting filters  $W_n$  and  $W_d$  should be adjusted to balance the effect of disturbance and measurement noise.

## REFERENCES

- [1] A. S. Saeed, A. B. Younes, S. Islam, J. Dias, L. Seneviratne, and G. Cai, "A review on the platform design, dynamic modeling and control of hybrid UAVs," in *2015 International Conference on Unmanned Aircraft Systems (ICUAS)*. IEEE, 2015, pp. 806–815.
- [2] P. Sinha, P. Esden-Tempski, C. A. Forrette, J. K. Gibboney, and G. M. Horn, "Versatile, modular, extensible vtol aerial platform with autonomous flight mode transitions," in *Aerospace Conference, 2012 IEEE*. IEEE, 2012, pp. 1–17.
- [3] A. Oosedo, S. Abiko, A. Konno, and M. Uchiyama, "Optimal transition from hovering to level-flight of a quadrotor tail-sitter uav," *Autonomous Robots*, pp. 1–17, 2017.
- [4] R. H. Stone, P. Anderson, C. Hutchison, A. Tsai, P. Gibbens, and K. Wong, "Flight testing of the t-wing tail-sitter unmanned air vehicle," *Journal of Aircraft*, vol. 45, no. 2, pp. 673–685, 2008.
- [5] R. Bapst, R. Ritz, L. Meier, and M. Pollefeys, "Design and implementation of an unmanned tail-sitter," in *Intelligent Robots and Systems (IROS), 2015 IEEE/RSJ International Conference on*. IEEE, 2015, pp. 1885–1890.
- [6] S. Verling, B. Weibel, M. Boosfeld, K. Alexis, M. Burri, and R. Siegwart, "Full attitude control of a vtol tailsitter uav," in *2016 IEEE International Conference on Robotics and Automation (ICRA)*. IEEE, 2016, pp. 3006–3012.
- [7] Y. Demitrit, S. Verling, T. Stastny, A. Melzer, and R. Siegwart, "Model-based wind estimation for a hovering vtol tailsitter uav," in *2017 IEEE International Conference on Robotics and Automation (ICRA)*. IEEE, 2017, pp. 3945–3952.
- [8] R. Ritz and R. D'Andrea, "A global controller for flying wing tailsitter vehicles," in *Robotics and Automation (ICRA), 2017 IEEE International Conference on*. IEEE, 2017, pp. 2731–2738.
- [9] X. Lyu, H. Gu, Y. Wang, Z. Li, S. Shen, and F. Zhang, "Design and implementation of a quadrotor tail-sitter vtol uav," in *2017 IEEE International Conference on Robotics and Automation (ICRA)*. IEEE, 2017, pp. 3924–3930.
- [10] X. Lyu, H. Gu, J. Zhou, Z. Li, S. Shen, and F. Zhang, "A hierarchical control approach for a quadrotor tail-sitter vtol uav and experimental verification," in *2017 IEEE/RSJ International Conference on Intelligent Robots and Systems (IROS)*. IEEE, 2017.
- [11] Y. Wang, X. Lyu, H. Gu, S. Shen, Z. Li, and F. Zhang, "Design, implementation and verification of a quadrotor tail-sitter vtol uav," in *2017 International Conference on Unmanned Aircraft Systems (ICUAS)*. IEEE, 2017, pp. 462–471.
- [12] W. H. Chen, J. Yang, L. Guo, and S. Li, "Disturbance-observer-based control and related methods an overview," *IEEE Transactions on Industrial Electronics*, vol. 63, no. 2, pp. 1083–1095, 2016.
- [13] B. Xu, "Disturbance observer-based dynamic surface control of transport aircraft with continuous heavy cargo airdrop," *IEEE Transactions on Systems, Man, and Cybernetics: Systems*, vol. 47, no. 1, pp. 161–170, 2017.
- [14] W. Liang, S. Huang, S. Chen, and K. K. Tan, "Force estimation and failure detection based on disturbance observer for an ear surgical device," *ISA transactions*, vol. 66, pp. 476–484, 2017.
- [15] M. Zheng, S. Zhou, and M. Tomizuka, "A design methodology for disturbance observer with application to precision motion control: An h-infinity based approach," in *American Control Conference (ACC), 2017*. IEEE, 2017, pp. 3524–3529.
- [16] S. H. Jeong, S. Jung, and M. Tomizuka, "Attitude control of a quad-rotor system using an acceleration-based disturbance observer: An empirical approach," in *2012 IEEE/ASME International Conference on Advanced Intelligent Mechatronics (AIM)*. IEEE, 2012, pp. 916–921.
- [17] H. Wang and M. Chen, "Trajectory tracking control for an indoor quadrotor uav based on the disturbance observer," *Transactions of the Institute of Measurement and Control*, vol. 38, no. 6, pp. 675–692, 2016.
- [18] S. J. Lee, S. Kim, K. H. Johansson, and H. J. Kim, "Robust acceleration control of a hexarotor uav with a disturbance observer," in *2016 IEEE 55th Conference on Decision and Control (CDC)*. IEEE, 2016, pp. 4166–4171.
- [19] M. R. Mokhtari, B. Cherki, and A. C. Braham, "Disturbance observer based hierarchical control of coaxial-rotor uav," *ISA transactions*, vol. 67, pp. 466–475, 2017.
- [20] F. Zhang, X. Lyu, Y. Wang, H. Gu, and Z. Li, "Modeling and flight control simulation of a quadrotor tailsitter vtol uav," in *AIAA Modeling and Simulation Technologies Conference*, 2017, p. 1561.
- [21] D. Mellinger and V. Kumar, "Minimum snap trajectory generation and control for quadrotors," in *2011 IEEE International Conference on Robotics and Automation (ICRA)*. IEEE, 2011, pp. 2520–2525.
- [22] J. Zhou, X. Lyu, X. Gai, Z. Li, S. Shen, and F. Zhang, "Frequency domain model identification and loop-shaping controller design for quadrotor tail-sitter vtol uavs," in *2018 International Conference on Unmanned Aircraft Systems (ICUAS)*. IEEE, 2018 (accept).
- [23] N. H. Jo, H. Shim, and Y. I. Son, "Disturbance observer for non-minimum phase linear systems," *International Journal of Control, Automation and Systems*, vol. 8, no. 5, pp. 994–1002, 2010.
- [24] H. T. Seo, K. S. Kim, and S. Kim, "General design of disturbance observer for stable linear time-invariant single-input/single-output systems via an  $H_\infty$  approach," in *American Control Conference (ACC), 2017*. IEEE, 2017, pp. 3108–3113.
- [25] K. Zhou, J. C. Doyle, K. Glover, et al., *Robust and optimal control*. Prentice hall New Jersey, 1996, vol. 40.
- [26] L. Meier, D. Honegger, and M. Pollefeys, "Px4: A node-based multi-threaded open source robotics framework for deeply embedded platforms," in *2015 IEEE International Conference on Robotics and Automation (ICRA)*. IEEE, 2015, pp. 6235–6240.